International Conference on Space Optics—ICSO 2012

Ajaccio, Corse

9–12 October 2012

Edited by Bruno Cugny, Errico Armandillo, and Nikos Karafolas

Evaluation of InGaAS array detector suitability to space environment

L. Tauziede

K. Beulé

M. Boutillier

F. Bernard

et al.

International Conference on Space Optics — ICSO 2012, edited by Bruno Cugny, Errico Armandillo, Nikos Karafolas
Proc. of SPIE Vol. 10564, 105640O · © 2012 ESA and CNES · CCC code: 0277-786X/17/$18 · doi: 10.1117/12.2309217

Evaluation of InGaAS array Detector Suitability to space environment

L. Tauziède, K. Beulé, M. Boutillier, F. Bernard
Centre National d'Etudes Spatiales (CNES)
Toulouse, France

J.L. Reverchon
Alcatel-Thales-III-VLab
Palaiseau, France

A. Buffaz
Pleiades Technologies
Sassenage, France

Abstract— **InGaAs material has a natural cutoff wavelength of 1.65µm so it is naturally suitable for detection in Short Wavelength InfraRed (SWIR) spectral range. Regarding Earth Observation Spacecraft missions this spectral range can be used for the CO2 concentration measurements in the atmosphere. CNES (French Space agency) is studying a new mission, Microcarb with a spectral band centered on 1.6µm wavelength. InGaAs detector looks attractive for space application because its low dark current allows high temperature operation, reducing by the way the needed instrument resources. The Alcatel Thales III-VLab group has developed InGaAs arrays technology (320x256 & 640x512) that has been studied by CNES, using internal facilities. Performance tests and technological evaluation were performed on a 320x256 pixels array with a pitch of 30µm. The aim of this evaluation was to assess this new technology suitability for space applications. The carried out test plan includes proton radiations with Random Telegraph Signal (RTS) study, operating lifetest and evolution of performances as a function of the operating temperature.**

Keywords : InGaAs, proton irradiations, RTS, SWIR

I. INTRODUCTION

The goal of this study was to assess the InGaAs technology developed by French laboratory III-VLab. The target spatial application Microcarb [1] has the particularity to observe low light levels and has to be compatible with a microsatellite platform so that resources are limited. The choice of every device is very crucial. High temperature operation of InGaAs detectors is by the way very interesting for such a mission. That is why we studied this InGaAs technology suitability for space applications. The study involves samples focal plane arrays manufactured in pre-development context and coming from different lots, having therefore different characteristics. The results must not be considered as covering the whole production of this technology. Tested modules named "Cactus" format is 320x256 pixels with 30µm x 30µm photodiode. Sensitive spectral range is between 0,9µm and 1,65µm. 4 outputs are available which provide a 346Hz frame rate. The readout circuit can switch between 2 storage capacitors in order to adapt the total charges handling capacity. The package is hermetically sealed with a 1mm sapphire window and includes a getter and a single stage ThermoElectric Cooler (TEC) module inside.

II. INGAAS TECHNOLOGY

The InGaAs technology studied results from material growth of InGaAs on InP that has been studied in III-VLab for several decades from PIN photodiodes, lasers or avalanche photodiodes. Extensive work has been done using various growth techniques such as MetalOrganic Vapor-Phase Epitaxy (MOVPE). The material's quality and the interface states have been particularly studied [2]. As a result, MOVPE grown InGaAs/InP interfaces have continuously been improved.
N-doped InP substrates are commonly used due to lowest density of defects. A n-doped InP overgrowth provides a common cathode contact to the photodiode array.
We have chosen a standard heterostructure with 3 µm of active layer lattice matched on InP substrate. A n-doped InP layer with 1 µm of thickness is grown on it. P doping is obtained by using Zn diffusion across the InP cap layer. Diffusion mechanisms are governed by complex mechanism and contribute to the abruptness of the doping profiles [3, 4].
P-N junction in the InP isolates PIN photodiodes across the 2D array (Fig. 1). This 2D photodiode array is a planar structure that avoids mesa edge leakage. Moreover, surface's passivation and interface states are finely controlled.

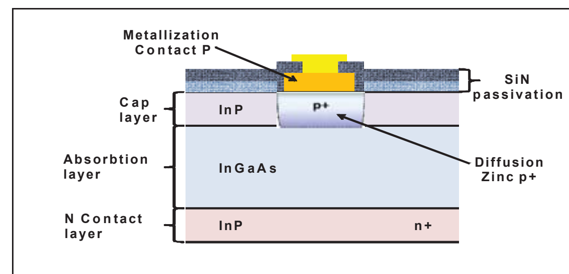

Figure 1. Schematic cross section of the planar InP/InGaAs photodiode: n^+-doped InP substrate, n^--doped InGaAs absorber layer and n-doped InP cap layer. The P-doping is obtained by Zn diffusion

The continuous improvement in process has determined diffusion and Shockley-Read-Hall (SRH) currents as the main contribution to dark current. This dark current is proportional to the photodiode diameter for small pixels. Thermal activation experiments reveals that the current contribution proportional to the photodiode area is diffusion limited even for bias up to 5 V, meaning that no or few SRH mechanism takes place in the depleted region. It shows the bulk InGaAs good quality. On the contrary the perimeter contribution dominating for small pixels shows both diffusion and SRH mechanism when bias increases [5]. The latest takes place at the interface between InGaAs and InP window layer. More generally, the diffusion current below the theoretical limit has been explained by a minority carrier (hole) concentration bellow equilibrium with small pitch photodiode arrays [6]. The continuous improvement of processing results in a dark current as low as 50 fA range at a reversed bias of 0,2 V at room temperature for a pixel size of 30µm × 30 µm.
In terms of QE, samples show a diffusion length of minority carriers larger than 60 µm, i.e. larger than the 30 µm pitch. This value is a typical value for InP / n-doped InGaAs / InP double heterostructure [7]. As a consequence, the minority carriers, holes, are all collected by the p contact. It is confirmed by the independence of responsivity versus bias. The strong electric field occurring at junction prevents the loss of spatial resolution that could be induced by such a high diffusion length. The minority carrier concentration is never at equilibrium and a drift current is always present. The only limitation of quantum efficiency is substrate transmission and anti reflection. That is why the substrate is thinned in order to limit free carriers absorption.

The first 1/4 TV format (320 × 256, 30 µm pitch) SWIR detection module "Cactus" based on an off-the shelf ISC 9809 ReadOut Integrated Circuit (ROIC) from FLIR Indigo was achieved successfully in 2008. The performance was at the state of the art in term of pixel operability (> 99%), dark current (<10 nA/cm2 @300 K) and quantum efficiency (> 70%).
All focal plane arrays involved in this study are manufactured from epilayers grown on lattice matched material at growth temperature. The cut-off wavelength is between 1,6657 and 1,6787 µm as shown on Fig. 2.

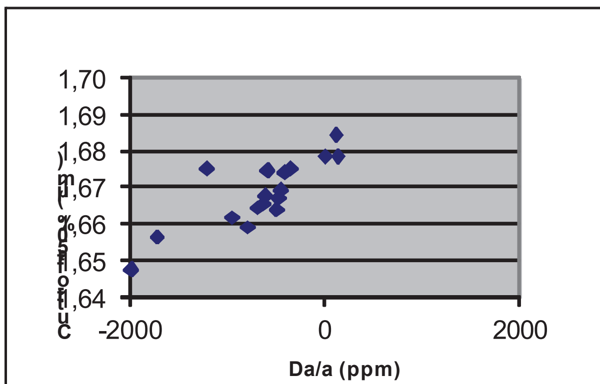

Figure 2. Typical relation between cut-off wavelength and lattice matching

Most of modules presented a dark current from 70 fA to 120 fA with compressive state from 0 to –600 ppm at room temperature. Now, dark currents bellow 50fA are currently achieved. Nevertheless, the density of threading dislocations is particularly low in order to decrease the random telegraphist noise effect well known for space applications. Indeed, lattice-mismatched photodiodes have shown high sensitivity to proton irradiation when biased in space operation [8]. Several studies suggest that RTS noise is due to excess current which flows through a crystalline defect and is modulated by an action of a small lattice defect [9]. In the case of lattice mismatched material employed for linear array with wavelengths cut-off larger than 1.7 µm, dislocations were incriminated [10].

III. TESTS CONDITIONS

An evaluation test plan has been defined to address proton irradiation and lifetest. Fig. 3 shows the evaluation test plan we followed.
Before protons irradiation and life tests, modules have been screened by applying 10 thermal cycles from -35°C to +85°C with modules powered off (made at Cdetech Toulouse laboratory) and a burn-in during 240 hours at +70°C with modules powered on and clocked.
The purpose of the evaluation was to assess the technology but not the package which explains why assembly tests were not performed.

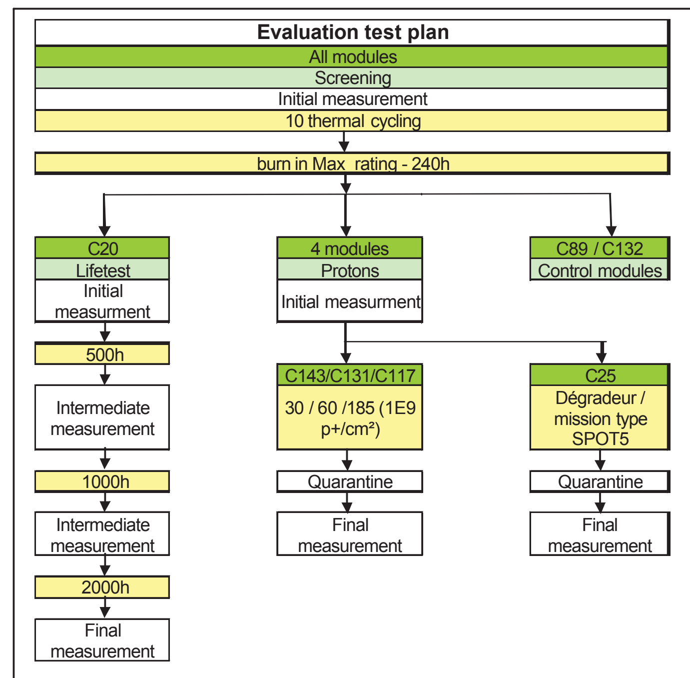

Figure 3. Evaluation test plan

A. Protons test conditions

Considering InGaAs sensitivity to displacement damages, lessons learned for example on Spot 4 [8], proton irradiation is considered critical for this material regarding space applications. Given the observed limitation of protons effects with bias voltage reduction on Spot 4, we assumed bias voltage interaction with results. So in order to be in the same conditions as during a space mission, tested modules were irradiated powered on at -0.5V bias voltage (standard bias condition for this device). Consumption was monitored during the tests and protective electronic was designed to turn off power in case of current increase to protect ROIC from any destructive latch-up.

The proton test plan was driven by classical test (high and low energy) and to be more representative of a true proton spectrum we also decided to introduce a new test based on a "Degrader" facility developed by TRAD/CNES.
Four modules were irradiated with test conditions described in Table I. Lower energy tests took place at Université Catholique de Louvain (UCL), Belgium and high energy and Degrader tests at Kernfysisch Versneller Instituut (KVI), Netherlands.

Three of them were irradiated with mono-energetic beam with the same fluence of 1e11 p+/cm² but at energies of 30, 60 and 185 MeV respectively. The fourth one has been irradiated using 185 MeV mono-energetic beam coupled with the degrader facility. This degrader is a specific facility enabling protons deposition of an energy spectrum representative of real flight conditions. The energy spectrum is calculating from orbital parameters. For this particular irradiation, the energy spectrum corresponds to 10 years of the chosen target mission MicroCarb as defined during preliminary study [1]. Parameters describing the orbit are summarized in Table II. Such parameters lead to an equivalent fluence of 1.5e10 p+/cm² 60 MeV protons.

TABLE I. PROTON IRRADIATION CONDITIONS

Module	Energy	Facility	Fluence	Flux	Duration	Polarization
C143	30 MeV	UCL	$1^{E}11$ p+/cm²	$1.29^{E}8$ p+/cm²/s	12 min 33s	**-0.5 V**
C131	60 MeV	UCL	$1^{E}11$ p+/cm²	$1.33^{E}8$ p+/cm²/s	12 min 56s	**-0.5 V**
C117	185 MeV	KVI	$1^{E}11$ p+/cm²	$2.5^{E}8$ p+/cm²/s	6 min 39 s	**-0.5 V**
C25	Degrader	KVI	Microcarb mission spectrum, 10 years, 3.75 mm shielding	Init = $1^{e}8$ p+/cm²/s 3 flux divisions	120min	**-0.5 V**

TABLE II. MICROCARB MISSION ORBIT

Orbit altitude	≈ 700 / 705 km
Local time at ascending node	13h30
Inclination	≈ 98,188 deg (heliosynchronous orbit)
Eccentricity/Perigee	0,001
Revisit time/ orbits	16 days – 233 orbits

E/O optical tests were performed before and after proton irradiations.

B. Lifetest conditions

In order to fit normalized lifetest procedure, we decided to proceed to 2000h lifetest. Given manufacturer information about operating temperature range between -10°C to +70°C, we decided to carry out the first steps at the maximum tested temperature +70°C and to do the last 1000 hours test at 85°C as shown on Fig. 4.

Figure 4. Lifetest procedure

However, due to limitations in the number of available devices, only one device was tested in lifetest. This device is referenced as C20. During whole lifetest, device C20 was powered and clocked. The consumption was monitored. Internal facilities were used to carry out this subgroup.
As already mentioned the tests were performed after screening of the modules.

C. E/O optical benches facilities

Performance tests and initial/final measurements were performed at CNES using 2 benches. For this device evaluation we developed an optical bench and a cooling bench adapted for Cactus electrical and mechanical interfaces.

1) Control bloc

A common bloc for the 2 benches allows detector powering, clocking, image acquisition and processing. It is composed of an electronic board, a temperature controller, a pattern generator and a 16 bits analog to digital converter all monitored by a computer.

2) Optical bench

The optical bench provides a calibrated incident luminance which is necessary for response and non linearity measurements. This bench uses a 150W tungsten lamp, an objective, a spectral filter and an integrating sphere with a calibrated photodiode to monitor light flux.

3) Cooling bench

In order to work with varied operating temperatures conditions, we used a vacuum chamber shown on Fig. 5 with inner cooling equipment composed by a TEC and cold liquid circulation. The module is under vacuum in order to avoid water vapour condensation and short circuits generation. The chamber has an IR grade fused silica 50mmdia x 8mm window allowing E/O optical tests. This facility enables temperature cooling down to 253K (-20°C) with one device operating. Temperature of device and elements of the system are monitored through dedicated sensors. Fine temperature regulation is made by the TEC associated with a Proportional–Integral–Derivative (PID) controller. System stability (especially temperature stability for dark current measurement) and operability was checked by dedicated measurements before starting the evaluation tests.

Figure 5. Vacuum chamber with Cactus mounted inside before vacuum pumping

D. Measurement methods

1) Dark current and non uniformity

Dark current is measured by varying integration time t_{int} at a given temperature in dark conditions on the cooling bench and calculated with (1).

$$S_{Dark} = \frac{I_{Dark}.CVF.G_{Elec}}{q}.t_{\text{int}} + S_{Offset} \quad (1)$$

With S_{Dark} the measured signal in the dark in Least Significant Bit (LSB) representative to the quantization step, I_{Dark} the dark current in Ampere units, CVF the Charge to Voltage Factor in V/é, G_{Elec} the video chain factor in LSB/V, q the electron charge in Coulomb and S_{Offset}, the offset signal in LSB.

We observed CVF dispersion between modules so we measured it on each module and used this measured value for dark current calculation.

2) Charge to voltage factor

CVF estimation is performed under light flux in order to limit regulation temperature noise and is calculated with (2).

$$\sigma^2{}_{tot} = CVF.G_{Elec}.(S_{tot} - S_{Offset}) + \sigma^2{}_{ROIC} + \sigma^2{}_{Elec} \quad (2)$$

With σ^2_{tot} the total temporal variance over images acquisitions for each pixel of the array in LSB, σ^2_{ROIC} and σ^2_{Elec} respectively the squared ROIC and video chain noises in LSB and S_{tot} the measured signal in LSB for each pixel.

Dark Signal Non Uniformity (DSNU) is defined by (3) :

$$DSNU_{i,j} = \frac{I_{Dark\,i,j} - \overline{I_{Dark}}}{\overline{I_{Dark}}} \quad (3)$$

with $I_{Dark\,i,j}$ the (i,j) pixel dark current and $\overline{I_{Dark}}$ the mean dark current of the array.

3) Response and non uniformity

The response and Pixel Response Non Uniformity (PRNU) are measured for -0.2V bias voltage on the optical bench with a high pass filter with a 1.5µm low cut-off so that spectral domain is limited by the detector cut-off for the upper wavelength.

The PRNU is defined by (4):

$$PRNU_{i,j} = \frac{S_{i,j} - \overline{S}}{\overline{S}} \quad (4)$$

with $S_{i,j}$ the (i,j) pixel signal under light and $\overline{S}$ the mean signal on the array.

IV. PERFORMANCES

A. Dark current

For most space applications, we try to limit dark current so that it is not the main noise contributor. In particular for Microcarb mission, the goal of limiting dark current is to be able to use this device at high operating temperature. This way, we reduce the resources needed on such microsatellite compatible mission [1]. That is why, it is interesting to study which parameters reduce that current in this InGaAs technology in order to be able to choose the best operating point. We studied reverse bias voltage level, temperature and irradiation influence on dark current.

1) Dark current vs bias

The optimal bias voltage for InGaAs is known to be close to 0V but the ROIC used in this device do not allow auto-nulling which maintains the photodiodes close to zero, the standard bias voltage is -0.5V.

We tested bias voltage effect on dark current in -0.3V to -0.8V range and at 2 operating temperatures as shown on Fig. 6.

We observe a linear relation of dark current density with bias voltage. The gradient differs for each temperature with an exponential relation as we will see hereafter.

Dark current decreases with lowering polarization, this confirms the interest of a bias voltage close to 0V for InGaAs technology. As far as this device is concerned, we would recommend using it at -0.2V bias voltage for spatial mission such as MicroCarb.

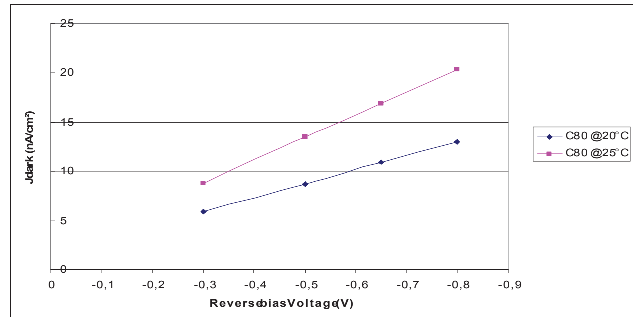

Figure 6. Dark current density as a function of bias voltage on C80 module

2) Dark current vs temperature

We measured a non irradiated component C80 in the range 253K – 298K at -0.5V bias voltage but we observed non linearity at low temperature and high integration times (few seconds), so we only work on the linear part, over 273K.

As we can see on Fig. 7, the measurements performed at different temperatures confirm that dark current follows an exponential function.

Considering a relation given as Jdark proportional to $T^{3/2}$.exp(-Eact/(k.T)), we can deduce an activation energy of 0.56 eV.

We have to notice that we observe dark current at -0.5V bias voltage which is not the optimal polarization and induces others current contributions than diffusion current.

3) Dark current vs protons

As discussed before, InGaAs is used to be sensitive to displacement damages. In space environment, proton irradiation can be an issue because during satellite life, devices are exposed to radiations. If the component is sensitive, those radiations will generate defects in the device which produce dark current.

In order to evaluate this InGaAs sensitivity to protons irradiation, four devices were used. Irradiations conditions are presented in Table 1 (see §III).

Devices were polarized and consumption was recorded during radiations. No change in consumption was observed during radiations, meaning that no protons induced single events occurred during radiation runs.

For each device, dark current was measured before and after proton irradiation for -0.5V bias voltage.

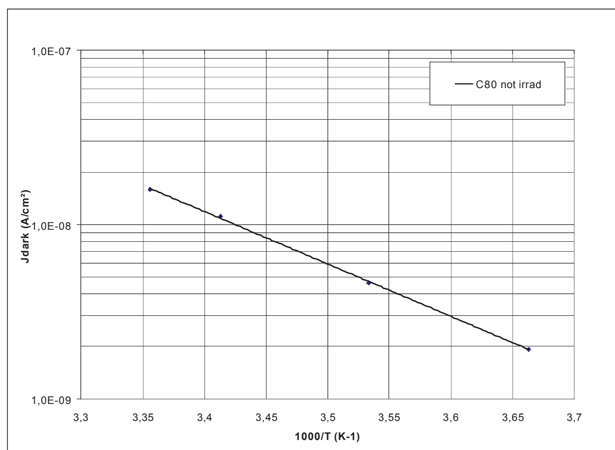

Figure 7. Dark current density as a function of temperature for C80 module with a logarithmic unit axis

First, an increase in mean dark current value is observed. Secondly the apparition of a distribution tail is noticed after irradiations. Those two effects can be seen on dark current histograms shown on Fig.8 and Fig.9.

Table III presents the mean dark current of the array as well as the DSNU, both before and after irradiations for the four tested modules at 298K. As expected in this range of energies, the lower the energy the higher is the degradation in mean dark current.

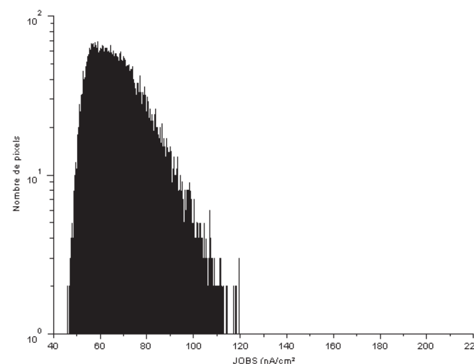

Figure 8. Dark current density of C25 module before proton irradiation

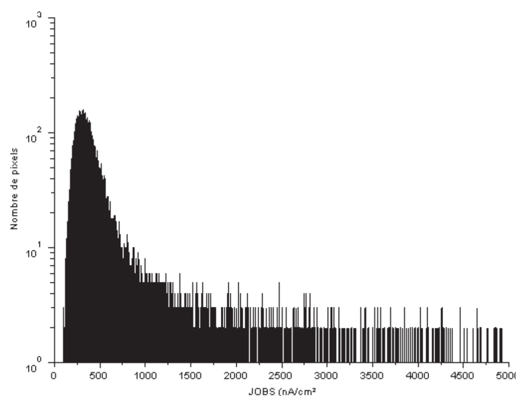

Figure 9. Dark current density of C25 module after proton irradiation with "Degrader" facility

TABLE III. DARK CURRENT AND DSNU EVOLUTION. "PIC" JOBS REPRESENT THE DARK CURRENT OF THE MOST LARGE POPULATION

Module	Energy (MeV)	Pic Jobs before (nA/cm²)	Pic Jobs after (nA/cm²)	Mean Jobs before (nA/cm²)	Mean Jobs after (nA/cm²)	DSNU before (%)	DSNU after (%)
C 117	185	34,4	245,6	34, 6	1272	2.2	235
C 131	60	22	751	26,6	1720	31,6	100,9
C 143	30	28,5	5791	30	6043	6,4	13,6
C 25	Dégradeur	58	280	67,1	468	16	117

Looking more in details to the degrader radiations results which is representative of the target MicroCarb mission, it appears that the "pic" dark current increases by a factor 5. At the same time, a DSNU increase from 16% to 117% is observed. Dark current distributions of C25 device before and after radiation are presented on Fig. 8 and Fig.9.

Dark current and DSNU increase after irradiations is too important for spatial application such as MicroCarb mission that is why we studied how operating conditions can reduce dark current and spatial dispersion such as operating temperature, integration time and bias voltage.

The dark current has been studied as a function of temperature only after irradiation and for 2 different bias voltages on the C25 module.
Fig. 10 shows that proton irradiation induces an increase in dark current density but with the same activation energy as for module C80 which was not irradiated. As a comparison, dark current evolution is plotted for a device from Xenics [10]. We can see that the activation energy tends to be the same. The dark current is lower than for C25 module because auto-nulling is provided for Xenics device.
A hypothesis could be that this identical activation energy is the result of the same phenomenon for both non irradiated and irradiated Cactus components.
We can deduce from Fig. 10 that to keep the same dark current as before radiation at 298K, for instance, we have to decrease the operating temperature to 278K.

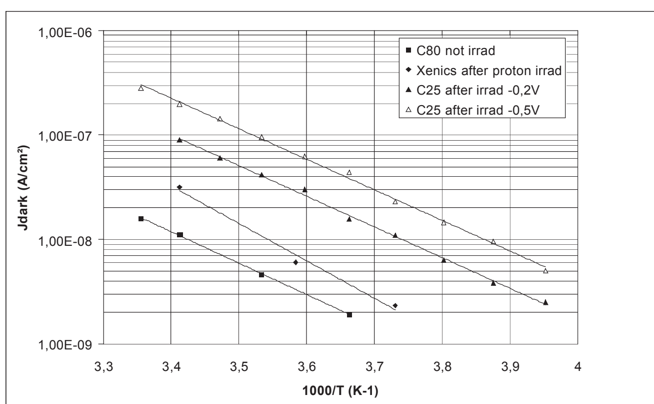

Figure 10. Dark current evolution with operating temperature for both irradiated and non irradiated devices

Studying only the "pic" or mean dark current evolution is not sufficient, we are also interested in DSNU comportment and origin. Indeed, the increase of DSNU after irradiation shows that some pixels get noisier that is why we also studied RTS presence.

B. *RTS study after proton irradiation*

RTS phenomenon is difficult to observe according to operating conditions and measurement facility. Indeed, RTS steps can be hidden by temporal noise. That is why we paid attention to develop particular methodology of measurement with short time between acquisitions and fine temperature stability. Moreover edge detection technique described in [11] has been used in order to count RTS pixels. The convolution of a normalized step shaped filter and the dark signal of each pixel allows the detection of the edges generated by the RTS phenomenon. The filter length used was not enough to attenuate the white Gaussian noise of dark signal so we modified the threshold criteria value given in [11] to avoid false alarms. We experimentally chose to multiply it by 5 so that we did not observe false alarms. We have to notice that this choice can affect the amount of detected RTS pixels but the amplitude of the phenomenon study got sense considering the criteria is fixed for the whole configurations.

Our study deals with the peak to peak dark signal amplitude of RTS pixels also named RTS step amplitude in this paper and its relative amplitude in regards with its mean dark signal as defined on Fig. 11.
We observed an apparition of RTS pixels on arrays (homogenous on the area) so we further study only a window of 80 by 64 pixels.
Moreover we observed the RTS phenomenon for 3 reverse bias voltages. Table IV reveals that pixels showing RTS step amplitude higher than 3 times theoretical noise (square root of the mean dark signal without RTS) are independent from reverse bias voltage level.

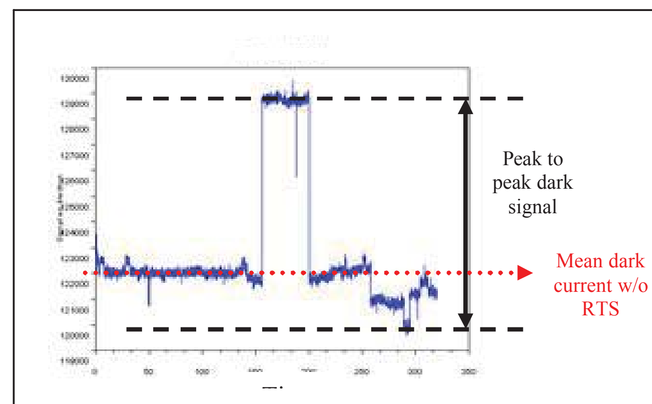

Figure 11. Dark signal signature of a RTS pixel according to time

TABLE IV. RTS PHENOMENON AS A FUNCTION OF THE REVERSE BIAS VOLTAGE ON C25 MODULE AT 298K

Bias (V)	Integration time (ms)	Nb of RTS pixels (%)	Nb of RTS pixels > 3 times noise (%)	Nb of RTS pixels > 6 times noise (%)
-0.3	2	7.6	5,3	3,6
-0.5	2	8	5,3	3,3
-0.8	2	8.2	5,2	3,2

We choose then to study RTS phenomenon for -0.2V bias voltage.

1) RTS vs temperature

We first studied the amplitude of RTS step as a function of temperature as shown on Fig. 12. The considered RTS step amplitude is the mean RTS step amplitude of all RTS pixels. It is measured for one integration time (16ms) at different temperatures. The RTS step amplitude of each pixel is defined as the peak to peak amplitude of the dark current of each pixel.

We can notice that at a given integration time, the RTS step amplitude increases with temperature and this increase is much higher when the integration time increases. Fig. 13 shows that the amount of RTS pixels also increases with temperature.

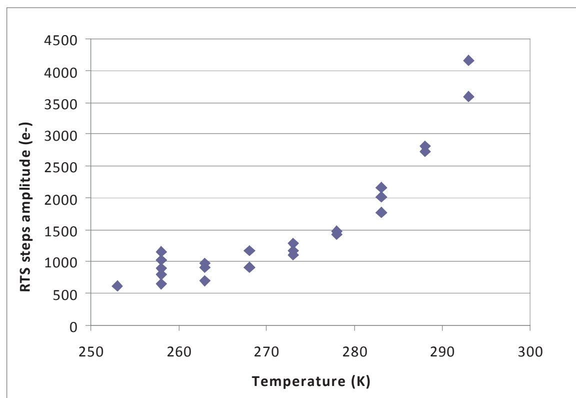

Figure 12. RTS amplitude as a function of temperature

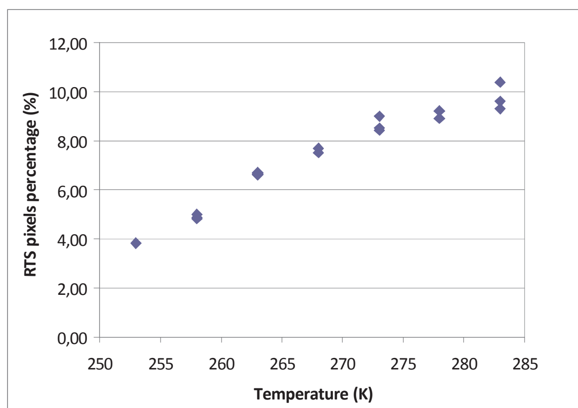

Figure 13. Percentage of RTS detected pixels as a function of operating temperature for the C25 module

Those measurements show some induced RTS phenomena on C25 device. In details characterization of pixels presenting RTS reveals that the RTS step amplitude as well as the amount of pixel impacted are increasing with temperature. Moreover RTS step amplitude seems to present the same trend as dark current with temperature so we analyzed this amplitude in relation with dark current.

As we can see on Fig. 14, RTS step amplitude stays in between 1% to 3% of dark signal for the whole temperature range.

For spatial mission, this 3% of dark current random step can be an issue because we compare calibration data with measurement data. RTS can appear on the measured data whereas it was not on the calibrated measurement. This induces an error on the calibrated data we obtain.
In order to limit this randomly phenomenon, those tests show that the solution is to reduce operating temperature according to accuracy requirement of the application.

2) RTS vs integration time

Then the RTS was observed as a function of integration time. Fig. 15 shows an increase in the RTS amplitude with integration time.

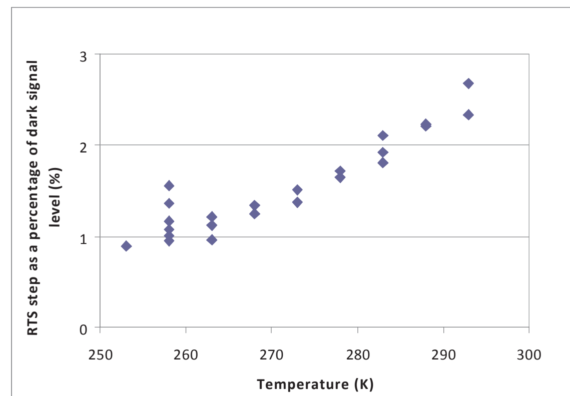

Figure 14. RTS amplitude as a percentage of dark current

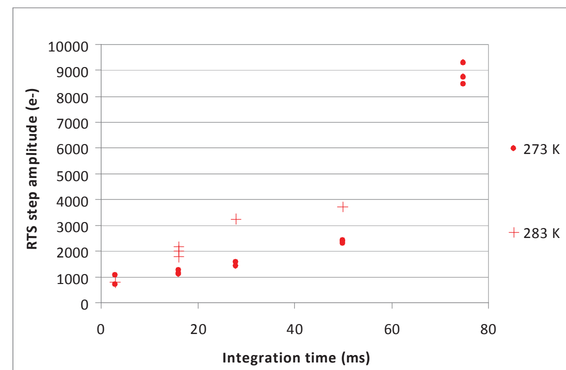

Figure 15. RTS amplitude as a function of integration time

As far as MicroCarb mission is concerned, decreasing integration time is not an option because low light levels are observed.

We can assume that the material defect inducing RTS acts as a trap for charges. These created RTS centers present an activation energy that is why an increase in integration time and temperature causes an increase in RTS step amplitude.

Those parametric studies on RTS phenomenon confirm that reducing operating temperature enables limiting RTS defects.

C. Lifetest results

During lifetest, an evolution of the bench configuration occurred between initial and intermediate measurements.

We decided only to compare the first intermediate measurement with the further ones. Table V shows that no dark current nor DSNU evolution occurred during 500 hours at 70°C and 1000 hours at 85°C.

Measurement under light flux did not show impact neither on sensitivity nor on pixel response non uniformity (Table VI).

This lifetest shows that Cactus performances are not degraded after 500 hours at 70°C and 1000 hours at 85°C, this is encouraging for using this technology for space applications. Moreover, we were able to operate the C25 module during few hours at -20°C, this tends to show that Cactus can be operated at lower temperature than datasheet range temperature which can be useful for space applications.

TABLE V. DARK SIGNAL EVOLUTION DURING LIFETEST

T (K)	Step	Mean dark current (nA/cm²)	DSNU (%)
298	500 H	26,1	2,61
	1000 H	27,1	2,55
	Final (2000 H)	26,9	2,56

TABLE VI. PRNU EVOLUTION DURING LIFETEST

T (K)	Step	PRNU (%)
290	Initial	-1,80
	Final	-1,69
298	Initial	-1,89
	Final	-1,70

V. CONCLUSION

This study provides some guidelines concerning the use of this InGaAs technology for space applications, more precisely for Microcarb mission. The particularity of the mission is first that it aims at observing low light levels and then that it has to be compatible with a microsatellite platform so the available resources are limited.

First, we can notice that dark current decreases with lowering polarization, which confirms the interest of a bias voltage close to 0V for InGaAs technology.

The results presented in this paper also confirm that proton radiations impact dark current level and dispersion. We also were able to observe RTS phenomenon.
Decreasing the operating temperature enables decreasing both dark current level and RTS step amplitude. On the contrary, RTS step amplitude seems to be independent from bias voltage level.

As far as MicroCarb mission is concerned, this technology is suitable for spectral band centered on 1.6µm providing that operating temperature is chosen according to post irradiation data and bias voltage close to zero.
Still, proton irradiations should be performed on recent devices in order to determine the operating temperature allowing dark current level to be in agreement with Microcarb requirement. Moreover RTS characteristics such as time constant and step amplitude should be measured at this operating temperature.

The technology is also still under study at III-VLab in order to reduce dark current and to limit RTS centers apparition in the material.

REFERENCES

[1] C.Buil, V.Pascal, J. Loesel, C. Pierangelo, L.Roucayrol, L. Tauziede, “A new space instrument concept for the measurement of CO2 concentration in the atmosphere”, SPIE 8176-12 Remote Sensing Europe, Prague, 2011

[2] J. Decobert and G. Patriarche, “Transmission electron microscopy study of the InP / InGaAs and InGaAs / InP heterointerfaces grown by metalorganic vapor-phase epitaxy”, J. Appl. Phys. 92, 2002

[3] S. J. Taylor, B. Beaumont and J. C. Guillaume, “Diffusion of Zn across p-n junctions in $Ga_{0.47}In_{0.53}As$“, Semicond. Sci. Technol, 8, p643, 1993

[4] D.G. Deppe, “Thermodynamic explanation to the enhanced diffusion of base dopant in AlGaAs-GaAs npn bipolar transistors”, Appl. Phys. Lett. 56, 370, 1990

[5] E. De Borniol, F. Guellec, P. Castelein, A. Rouvié, J. A. Robo, J. L. Reverchon, “High-performance 640 x 512 pixel hybrid InGaAs image sensor for night vision”, Proc. SPIE 8353, 2012

[6] J. Trezza, N. Masaun, M. Ettenberg, “Analytic modeling and explanation of ultra-low noise in dense SWIR detector arrays”, Proc. SPIE 8012, 2011

[7] M. Gallant and A. Zemel, “Long minority hole diffusion length and evidence for bulk recombination limited lifetime in InP / InGaAs / InP double heterostructure”, Appl. Phys. Lett. 52, 1988

[8] S. Barde, R. Ecoffet, J. Costeraste, A. Meygret, and X. Hugon “Displacement damage effects in IngaAs detectors: experimental results

and semi-empirical model prediction", IEEE Trans. On Nuclear Science, Vol. 47, n°6, 2000

[9] Pogany et al., "Study of RTS noise and excess currents in lattice-mismatched InP / InGaAs / InP photodetector arrays", Solid-State Electronics, vol. 38, No. 1, pp. 37-49, 1995

[10] G. Hopkinson et al. "Radiation Effects in InGaAs and Microbolometer Infrared Sensor Arrays for Space Applications" IEEE transactions on nuclear science, Vol. 55, No. 6, 2008

[11] V. Goiffon, G. R. Hopkinson, P. Magnan, F. Bernard,G. Rolland, O. Saint-Pé, "Multilevel RTS in Proton Irradiated CMOS Image Sensors manufactured in a Deep Submicron Technology", IEEE transactions on nuclear science, Vol. 56, No. 4, 2009